Energy Conversion and Management 184 (2019) 436–447

Contents lists available at ScienceDirect

Energy Conversion and Management

journal homepage: www.elsevier.com/locate/enconman

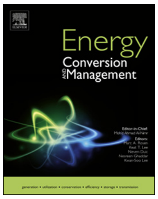

Pyrolytic kinetics, reaction mechanisms and products of waste tea via TG-FTIR and Py-GC/MS

Haiming Cai[a], Jingyong Liu[a,*], Wuming Xie[a], Jiahong Kuo[a], Musa Buyukada[b], Fatih Evrendilek[c,d]

[a] Guangzhou Key Laboratory of Environmental Catalysis and Pollution Control, Guangdong Key Laboratory of Environmental Catalysis and Health Risk Control, School of Environmental Science and Engineering, Institute of Environmental Health and Pollution Control, Guangdong University of Technology, Guangzhou 510006, China
[b] Department of Chemical Engineering, Bolu Abant Izzet Baysal University, Bolu 14052, Turkey
[c] Department of Environmental Engineering, Bolu Abant Izzet Baysal University, Bolu 14052, Turkey
[d] Department of Environmental Engineering, Ardahan University, Ardahan 75002, Turkey

ARTICLE INFO

Keywords:
Waste tea
Pyrolysis
Kinetic
Master-plots
TG-FTIR
Py-GC/MS

ABSTRACT

The present study experimentally quantified the pyrolysis behaviors of waste tea (WT) as a function of four heating rates using thermogravimetric-Fourier transform infrared spectrometry and pyrolysis-gas chromatography-mass spectrometry analyses. The maximum weight loss of WT (66.79%) occurred at the main stage of devolatilization between 187.0 and 536.5 °C. The average activation energy estimates of three sub-stages of devolatilization were slightly higher (161.81, 193.19 and 224.99 kJ/mol, respectively) by the Flynn-Wall-Ozawa than Kissinger-Akahira-Sunose method. Kinetic reaction mechanisms predicted using the master-plots were $f(\alpha) = (3/2)(1-\alpha)^{2/3}[1-(1-\alpha)^{1/3}]^{-1}$, $f(\alpha) = (1-\alpha)^2$, and $f(\alpha) = (1-\alpha)^{2.5}$ for the three sub-stages, respectively. The prominent volatiles of the WT pyrolysis were CO_2 > C=O > phenol > CH_4 > C–O > NH_3 > H_2O > CO. A total of 33 organic compounds were identified including alkene, acid, benzene, furan, ketone, phenol, nitride, alcohol, aldehyde, alkyl, and ester. This study provides a theoretical and practical guideline to meeting the engineering challenges of introducing WT residues in the bioenergy sector.

1. Introduction

Globally, the biomass feedstocks of bioenergy crops, and agricultural and forestry residues are considered to be the fourth largest resource of primary energy [1]. In particular, various biomass residues (e.g., pine sawdust, wheat straw, rice straw, and rice husk) have been explored as a renewable and clean energy resource to generate electricity, hydrogen, and liquid fuels [2,3]. For example, their use in bioenergy production via high-tech pathways such as pyrolysis has been relied on in restricting global mean temperature rise to 1.5 °C above pre-industrial by the end of this century [4–6]. Tea industry is considered to be the most common non-alcoholic beverage worldwide and produces large amounts of waste tea (WT). In 2015, the amount of the global tea production was 5.3 million tons 2.27 million tons of which were from China, and over 90% of which was left after consumption as WT [7,8]. The utilization potential of WT has been quantified in the domains of feeding animals [9], synthesizing silver nanoparticles [10], preparing microcrystalline cellulose [8], and developing an efficient adsorbent to remove mercury [11]. However, for generating bioenergy via pyrolysis, there exist a very few studies in related literature.

Pyrolysis of various biomass feedstocks such as para grass, wood sawdust, and moso bamboo has been studied owing to its energy efficiency and environmental advantages [12–14]. The fast pyrolysis of WT can also yield high bioenergy in the forms of char, liquid and gas productions [15]. However, to meet the engineering challenges of designing the WT pyrolysis process in the bioenergy sector necessitates the better quantification and understanding of its pyrolysis behaviors, kinetics and products [16,17].

Thermogravimetric (TG) analyses and estimates provide a guidance on the feasibility, design, and optimization of the sustainable bioenergy systems [4,18]. The use of the iso-conversional methods has led to the reliable estimation of the kinetic triplets of the apparent activation energy (E_α, kJ/mol), the pre-exponential factor (A), and the kinetic model $f(\alpha)$ [19]. Their model-free approaches such as Flynn-Wall-Ozawa (FWO), and Kissinger-Akahira-Sunose (KAS) cannot directly lead to a reaction kinetic model [20]. The model-fitting approaches can yield E_a and A estimates based on a priori knowledge of reaction mechanism functions [21]. For example, the master-plots constitute the theoretically baseline curves using differential $f(\alpha)$ as well as integral $g(\alpha)$ functions, regardless of E_a and A. The master-plots method depends

---

* Corresponding author.
E-mail address: Liujy@gdut.edu.cn (J. Liu).

https://doi.org/10.1016/j.enconman.2019.01.031
Received 31 October 2018; Accepted 13 January 2019

Nomenclature

WT	waste tea
β	heating rate (K/min)
TG-FTIR	thermogravimetric-Fourier transform infrared spectrometry
Py-GC/MS	pyrolysis-gas chromatography/mass spectrometry
E	apparent activation energy (kJ/mol)
A	pre-exponential factor (s^{-1})
R^2	coefficient of determination
α	conversion degree
T	the absolute temperature (K)
t	reaction time
FWO	Flynn-Wall-Ozawa method
KAS	Kissinger-Akahira-Sunose method
TG	mass loss
DTG	derivative mass loss
HHV	higher heating value
CO_2	carbon dioxide
CO	carbon monoxide
CH_4	methane
NH_3	ammonia gas
H_2O	water
3-D	three dimensional

on kinetic models instead of kinetic parameters of the process by comparing experimental master plots to theoretical ones, thus providing insight into the mechanism(s) of the pyrolysis process [22,23]. Thus, the model-free and model-fitting methods should be combined to estimate the kinetic parameters as well as the reaction mechanisms.

Thermogravimetric analysis coupled with Fourier transform infrared spectroscopy (FTIR) and pyrolysis-gas chromatography/mass spectrometry (Py-GC/MS) is the most common method to estimate the pyrolysis behaviors and products of biomass residues [24–28]. The main pyrolytic products identified using TG-FTIR were H_2O, CH_4, CO_2, CO, NO, NO_2, and carboxylic acids from moso bamboo [14]. The bio-crude-oil products were identified from Ceylon refused WT using TG-FTIR [29]. TG-FTIR was also used to determine the evolutions of gases from the pyrolysis process for WT [30]. The chemical characteristics and composition of theabrownin formed in Pu-erh teas were determined using Py-GC/MS [31]. However, the pyrolytic products released in the complex reactions have been found to be more accurately determined using the combination of TG-FTIR and Py-GC/MS analyses [32,33]. For example, Chen et al. [32] accurately estimated the co-pyrolysis products of *Chlorella vulgaris* and kitchen waste using both TG-FTIR and Py-GC/MS.

There exists a knowledge gap in related literature about bioenergy production via the pyrolysis of WT as an abundant feedstock. Therefore, the objective of this study was to quantify the pyrolysis degradation behaviors, kinetics and products for WT by using the combination of TG-FTIR and Py-GC/MS analyses.

2. Materials and methods

2.1. Sample preparation

Waste tea was produced from soaking tea leaves in 100 °C water for several times. Soaked WT was dried naturally under good ventilation for 24 h and then in an oven at 105 °C for 24 h for the further removal of moisture. The samples were grounded into 200 mesh before the experimental runs. The ultimate, proximate and higher heating value (HHV) analyses of WT are presented in Table 1. The components of WT were measured in triplicates using the wet chemistry method of Van Soest [20].

2.2. TG-FTIR experiments

A thermogravimetric analyzer (NETZSCH STA 409 PC Luxx) was used to quantify the non-isothermal pyrolysis behaviors of WT in the inert (100% N_2) atmosphere. The sample was heated from 30 to 900 °C at the four heating rates of 5, 10, 20 and 40 °C/min. The N_2 flow rate was held constant at 60 mL/min. The program control procedures of temperature-rise, atmosphere type, and gas flow rate were set beforehand. The initial sample masses were kept the same (6 ± 0.5 mg) for the analyzer in each experiment to ensure the comparability of the pyrolysis parameters. To ensure their repeatability, all the experimental runs were conducted at least twice.

Gases evolved from the pyrolysis process at 10 °C/min were detected using FTIR (Nicolet iS 50 FTIR spectrometer). FTIR spectra were observed at a rate of 8 scans per sampling at a resolution of 4 cm^{-1} in the wavenumber range of 4000 to 600 cm^{-1}. The purge and evolved gases from the TG pyrolysis furnace were transferred into the FTIR gas cell via a heated transfer line. The temperature of the capillary bundle was heated to 260 °C before the experiment to avoid the liquefaction of gases that passed through the capillary bundle. The test data were processed using the OMNIC software (Thermo Electron, USA).

2.3. Py-GC/MS experiments

Pyrolysis-gas chromatography/mass spectrometry was used to distinguish and identify the pyrolytic volatiles. At the pyrolysis stage, Frontier Lab PY-2020id was used as a pyrolysis reactor to conduct the pyrolysis at 600 °C for 24 s using purified He as the carrier gas. The volatiles products were separated using a chromatographic column with HP-5MS capillary (30 m × 0.32 mm × 0.25 μm) whose temperature was increased from 40 °C for 2 min to 300 °C for 10 min at a rate of 8 °C/min. The mass spectra were obtained in an electron ionization mode at 70 eV. The yields of the compounds were computed using the GC–MS spectra characterized according to the standard solution calibration, NIST library database, and previously published reports.

2.4. Kinetic analyses

The kinetic analysis can reveal the effect of reaction temperature and time on the thermal degradation during the pyrolysis process of a given biomass material [35]. The pyrolysis reaction kinetics can be stated thus:

Table 1
Ultimate, proximate and HHV analyses of WT.

Sample		WT	
Ultimate analysis (wt%, dry basis)	C	47.99 ± 0.04	[34]
	H	6.60 ± 0.04	
	O	28.73 ± 0.10	
	N	4.90 ± 0.07	
	S	0.18 ± 0.02	
Proximate analysis (wt%, dry basis)	Moisture	5.45 ± 0.03	
	Volatiles	82.31 ± 0.04	
	Ash	6.15 ± 0.06	
	Fixed carbon	6.09 ± 0.07	
Q_{net} (MJ/kg)		20.86 ± 0.33	
Composition	Hemi-cellulose	20.64 ± 0.23	
	Cellulose	7.06 ± 0.14	
	Lignin	20.04 ± 0.08	

O (wt%) = 100% − C − H − N − S − moisture − ash; Fixed carbon = 100 − moisture − ash − volatiles.

$$\frac{d\alpha}{dt} = k(T)f(\alpha) \tag{1}$$

where α, t, T, $k(T)$, and $f(\alpha)$ are conversion degree, reaction time, the absolute temperature (K), the reaction rate constant, and the reaction mechanism function, respectively. α and $k(T)$ can be determined using Eqs. (2) and (3):

$$\alpha = \frac{m_0 - m_t}{m_0 - m_f} \tag{2}$$

$$k(T) = A\exp\left(-\frac{E_a}{RT}\right) \tag{3}$$

where m_0, m_t and m_f is the initial, actual and final masses of the samples, respectively. R is the gas constant (8.314 J/K mol).

$\beta = dT/dt$, and combining Eqs. (1) and (3) leads to the following:

$$\frac{d\alpha}{dt} = \frac{A}{\beta}\exp\left(-\frac{E_a}{RT}\right)f(\alpha) \tag{4}$$

Performing the integration and transformation on Eq. (4) under the initial conditions ($\alpha = 0$, at $T = T_0$), Eq. (5) can be obtained thus:

$$\mathrm{G}(\alpha) = \int_0^{\alpha} \frac{d\alpha}{1-\alpha} = \int_0^{T} \frac{A}{\beta}\exp\left(-\frac{E_a}{RT}\right)\mathrm{dT} \tag{5}$$

The Eq. (5) is the basis of the most kinetic analyses employed in the related literature [36]. The reaction process is generally characterized combining the model-free and -fitting methods [22].

2.4.1. Iso-conversional methods

In this study, the model-free non-isothermal methods of Flynn-Wall-Ozawa (FWO) and Kissinger-Akahira-Sunose (KAS) were adopted to determine the apparent activation energy [36,37]. As proposed by Doyle's approximation, the FWO method can be stated thus [38]:

$$\ln\beta = \ln\left(\frac{AE}{RG(\alpha)}\right) - 5.3305 - 1.052\left(\frac{E_a}{RT}\right) \tag{6}$$

As developed according to Coats-Redfern approximation, the KAS method can be described as follows [39,40]:

$$\ln\left(\frac{\beta}{T^2}\right) = \ln\left(\frac{AR}{EG(\alpha)}\right) - \frac{E_a}{RT} \tag{7}$$

In the plots of $\ln\left(\frac{\beta}{T^2}\right)$ versus $1/T$, and $\ln\beta$ versus $1/T$, the slope of $-E_a/R$ yields the activation energy estimate.

2.4.2. Integral master-plots method

The master-plots serve to pinpoint the reaction models of the thermal degradations. In this method, the integrated form of Eq. (5) can be expressed as follow [41]:

$$G(\alpha) = \frac{AE}{\beta R}P(u) \tag{8}$$

where $u = E/RT$, and $P(u)$ is the temperature integral. $P(u)$ can be approximated using the empirical equations since it has no analytical solution. When the Tang–Liu–Zhang–Wang–Wang approximation is applied to the master-plots, the deviation of the numerical solution for $P(u)$ at $u > 14$ becomes less than 0.1% [42,43].

$$p(u) = \frac{exp(-u)}{u \times (1.00198882u + 1.87391198)} \tag{9}$$

For a single step degradation with a constant $G(\alpha)$, the appropriate kinetic model was confirmed using the master-plots where E_a and A values were estimated using $\alpha = 0.5$ as the baseline point. Thus, Eq. (8) was expressed as follows:

$$G(0.5) = \frac{AE}{\beta R}P(u_{0.5}) \tag{10}$$

where $u_{0.5} = E/RT_{0.5}$. G (0.5) is the integral reaction model at $\alpha = 0.5$; $T_{0.5}$ is the temperature at $\alpha = 0.5$.

The ratio of Eq. (8) to Eq. (10) can be expressed as follows:

$$\frac{G(\alpha)}{G(0.5)} = \frac{P(u)}{P(u_{0.5})} \tag{11}$$

This differential kinetic equation is among the most common applications of the Moment Propagation method.

Table 2 presents the most common reaction models—G (α)—of the thermal degradations. To obtain the best model, the theoretical $G(\alpha)/G(0.5)$ and experimental $P(u)/P(u_{0.5})$ values versus x were plotted, respectively. As can be seen in Eq. (11), for a given x, the $P(u)/P(u_{0.5})$ and $G(\alpha)/G(0.5)$ values are equivalent. If an inappropriate $G(\alpha)$ kinetic model was used, a greater difference between the theoretical versus experimental values would appear in the master-plots.

Table 2
The most common kinetic models, and their corresponding mechanisms for a solid state process [43].

Mechanisms	Symbol	$f(\alpha)$	$G(\alpha)$
Diffusion			
One-way transport	D1	$1/(2\alpha)$	α^2
Two-way transport	D2	$[-\ln(1-\alpha)]^{-1}$	$(1-\alpha)\ln(1-\alpha)+\alpha$
Three-way transport	D3	$(3/2)(1-\alpha)^{2/3}[1-(1-\alpha)^{1/3}]^{-1}$	$[1-(1-\alpha)^{1/3}]^2$
Ginstling–Brounshtein equation	D4	$(3/2)[(1-\alpha)^{-1/3}-1]^{-1}$	$(1-2\alpha/3)-(1-\alpha)^{2/3}$
Order of reaction			
First-order	F1	$1-\alpha$	$-\ln(1-\alpha)$
Second-order	F2	$(1-\alpha)^2$	$(1-\alpha)^{-1}-1$
Third-order	F3	$(1-\alpha)^3$	$[(1-\alpha)^{-2}-1]/2$
Random nucleation and nuclei growth			
Two-dimensional	A2	$2(1-\alpha)[-\ln(1-\alpha)]^{1/2}$	$[-\ln(1-\alpha)]^{1/2}$
Three-dimensional	A3	$3(1-\alpha)[-\ln(1-\alpha)]^{2/3}$	$[-\ln(1-\alpha)]^{1/3}$
Exponential nucleation			
Power law	P2	$2\alpha^{2/3}$	$\alpha^{1/2}$
Power law	P3	$3\alpha^{2/3}$	$\alpha^{1/3}$
Index law	P4	$4\alpha^{3/4}$	$\alpha^{1/4}$
Limiting surface reaction between both phases			
One dimension	R1	1	α
Two dimensions	R2	$2(1-\alpha)^{1/2}$	$1-(1-\alpha)^{1/2}$
Three dimensions	R3	$3(1-\alpha)^{2/3}$	$1-(1-\alpha)^{1/3}$

3. Results and discussion

3.1. Thermogravimetric analyses

As the initial stage of the combustion and gasification processes of a given biomass type mainly composed of (hemi-)cellulose, and lignin, the pyrolysis process plays an important role in determining ignition, flame stability, products, and burnout [44] as well as obtaining char, gas and bio-oil products at different temperatures [29,45]. The (D)TG curves of the WT pyrolysis in the N_2 atmosphere under the four heating rate are presented in Fig. 1. Fig. 1a and b showed that the (D)TG curves shifted towards the higher temperature with the increased heating rate, without affecting the pattern of the thermal degradation. This can be attributed mainly to the better heat transfer effect gained with lower sample particles [34,46]. Fig. 2 showed that the pyrolysis process of WT at 10 °C/min can be divided into the following three stages: drying at < 187.0 °C; devolatilization between 187.0 and 536.5 °C; and degradation of char and minerals > 536.5 °C.

The weight loss of WT was due to the evaporation of water at the low temperature in the first stage and corresponded to the range of 187.0 to 536.5 °C in the second stage of devolatilization (the main stage). The total weight loss of 66.79% in this main stage was related to the higher release of volatiles from the degradation of the organic compounds such as (hemi-)celluloses, partial lignin and other macromolecular substance as well as to the lower fixed carbon content of the sample. The peak fitting tool of Origin 9.0 was applied to divide the thermal degradation process of the main stage (devolatilization) into the three sub-stages, as was also applied to the thermal degradation of oily sludge, petrochemical wastewater sludge and hydrotalcite [22,42,43]. In the first sub-stage, the weight loss was mainly tied to the degradation of hemi-cellulose whose main degradation temperature was between 187.0 and 315.0 °C (Fig. 2). Hemi-cellulose with a lower degree of polymerization is a mixture of various polymerized monosaccharides such as xylose, mannose, glucose, galactose, and arabinose [15]. In the second sub-stage (315.0–385.0 °C), the weight loss was mainly due to the degradation of cellulose and part of lignin. Cellulose is a high-molecular compound with a long linear chain composed of D-glucosyl group [47] and has a crystalline structure made up of ordered microfibrils that renders its thermal degradation more difficult than that of hemi-cellulose [27]. In the third sub-stage (385.0–536.5 °C), the degradation of lignin and macromolecular substances was more difficult than that of (hemi-)cellulose due to its complex composition. The pyrolysis of hemi-cellulose, cellulose, and lignin was reported to mainly occur from 200 to 300 °C, 300 to 400 °C, and 200 °C until the end of the pyrolysis process, respectively [14]. The maximum weight loss rate of WT was estimated at 5.51%/min at 345.3 °C. The final stage (> 536.5 °C) appeared to stem from the slow thermal degradations of residuals such as chars, minerals, and ash as the part of the final solid residues [48]. The WT residues were estimated at 20.42% after the pyrolysis in the N_2 atmosphere.

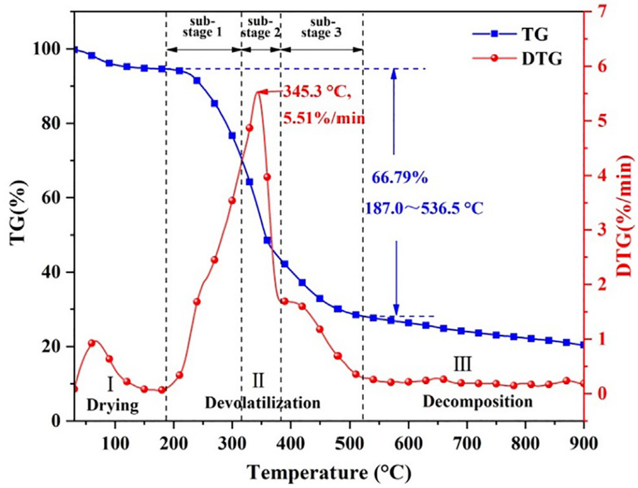

Fig. 2. (D)TG curves of WT pyrolysis at a heating rate of 10 °C/min.

3.2. Kinetics analyses

3.2.1. Apparent activation energy estimates

As recommended by the Kinetics Committee of the International Confederation for Thermal Analysis and Calorimetry [41], the parameter estimations of the microscopic pyrolysis reactions were based on the iso-conversional methods [14]. Since the thermal decompositions at the start and end of each stage were not stable, the conversion rate (α) was selected to range from 0.1 to 0.9 at an interval of 0.1 in order to better reflect changes in E_a values of WT. According to Eqs. (6) and (7), the E_a values for the three sub-stages of the main devolatilization stage of the WT pyrolysis were estimated using the FWO and KAS methods at the four heating rates. As showed in Fig. 3, the plots of ln β (FWO) and ln [β/T^2] (KAS) versus 1/T resulted in linear relationships for the given conversion degrees. The E_a estimates were derived from the slope of the regression lines (Table 3). The coefficients of determination (R^2) ranged from 0.9639 to 0.9996.

The average E_a estimates for the three sub-stages were slightly higher (161.81, 193.19 and 224.99 kJ/mol, respectively) by the FWO

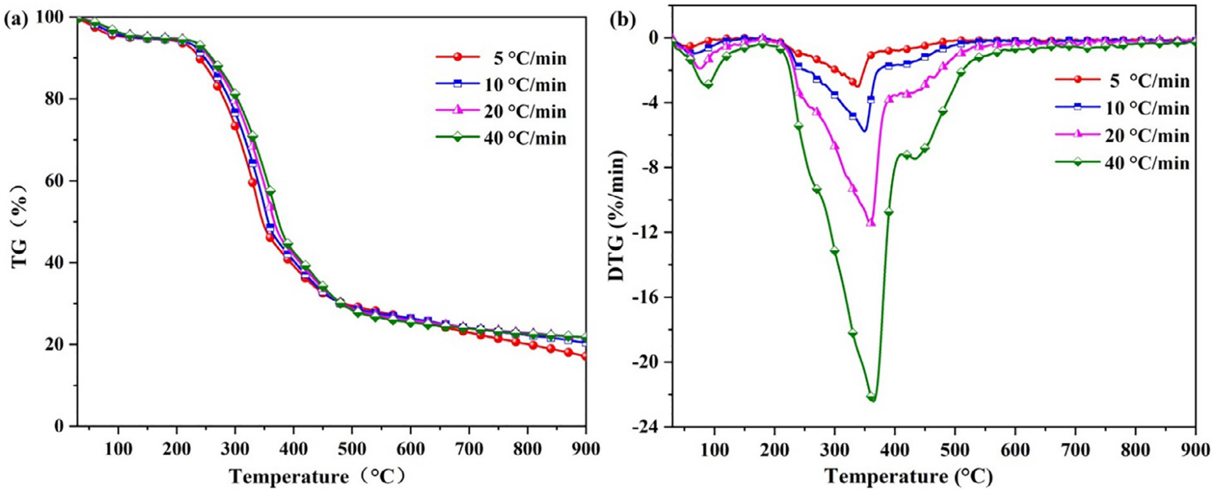

Fig. 1. (D)TG curves of WT pyrolysis at four heating rates: (a) TG and (b) DTG.

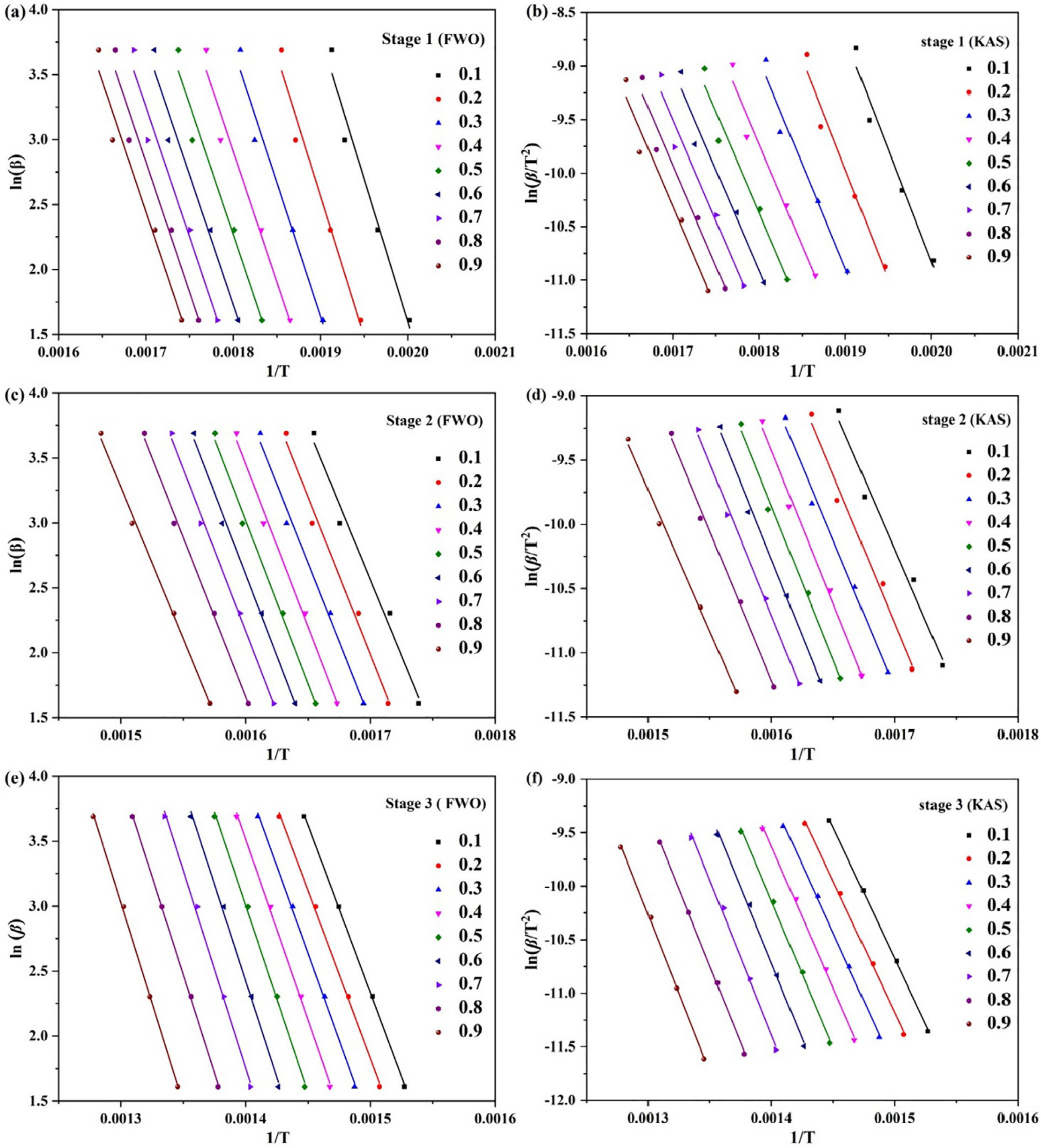

Fig. 3. Kinetic plots of three sub-stages according to FWO and KAS.

than KAS method. Since many different reactions in pyrolysis require different amounts of energy, the E_a value varied with the conversion degrees [49]. The first and second stages with the low and high E_a values were due to the thermal degradations of hemi-cellulose, and cellulose and partially lignin, respectively. Consistent with our finding, the E_a value was found to be higher in the thermal degradation of cellulose than hemi-cellulose [48]. The increased E_a in the third stage with the elevated temperature was due to the degradations of lignin, and coke with low reaction activity [15]. The increased E_a with the increased degree of pyrolysis at higher temperatures is consistent with the fact that the sample was more difficult to decompose [42]. The degradation process were found not to follow the same reaction mechanism [48]. Since the average E_a estimates by the KAS and FWO methods were very close, their average values (161.50, 193.06 and 224.79 kJ/mol) were adopted in the integral master-plots.

3.2.2. Reaction model by master-plots

In order for the complete reaction kinetics to be understood, the pre-exponential factor (A), the model, and the order of reaction (n) need to be estimated. The solid state kinetic models can be found using the master-plots when E_a is specified. The theoretical versus experimental master-plots are compared to obtain the most probable model [41]. Based on the predetermined E_a value, and the temperature measured as a function of α, $P(u)$ can be estimated directly according to Eq. (9). The plots of $P(u)/P(u_{0.5})$ versus α are shown in Fig. 4a–c. The $P(u)/P(u_{0.5})$ plots of each sub-stage under 5, 10, 20 and 40 °C/min were almost identical. This in turn suggested that the degradation kinetic mechanism was constant regardless of the heating rate and can be described using a single model [19].

The theoretical master-plots—$G(\alpha)/G(0.5)$—were computed using various kinetic functions (Table 2). The master-plots of $P(u)/P(u_{0.5})$

Table 3
Activation energy (E_a) estimates, and coefficients of determination (R^2) based on FWO and KAS for the three stages of the main WT pyrolysis.

Conversion (α)	Stage 1				Stage 2				Stage 3			
	FWO		KAS		FWO		KAS		FWO		KAS	
	E_a	R^2	E_a	R^2	E_a	R^2	E_a	R^2	E_a	R^2	E_a	R^2
0.1	173.69	0.9690	174.23	0.9661	184.92	0.9838	184.73	0.9821	204.06	0.9996	198.37	0.9995
0.2	171.01	0.9739	171.15	0.9713	191.79	0.9884	191.82	0.9872	204.39	0.9986	203.68	0.9984
0.3	162.83	0.9734	162.32	0.9705	191.72	0.9918	191.63	0.9909	211.73	0.9988	211.26	0.9986
0.4	159.10	0.9716	158.22	0.9683	197.98	0.9938	198.09	0.9931	219.85	0.9985	219.66	0.9984
0.5	158.17	0.9688	157.08	0.9652	198.64	0.9950	198.67	0.9945	227.70	0.9980	227.75	0.9977
0.6	157.00	0.9687	156.45	0.9650	198.44	0.9960	198.36	0.9956	234.71	0.9973	234.95	0.9969
0.7	157.67	0.9681	156.85	0.9643	197.18	0.9968	196.92	0.9964	240.00	0.9969	240.33	0.9966
0.8	158.02	0.9678	157.10	0.9639	193.64	0.9968	193.05	0.9965	238.37	0.9995	241.25	0.9994
0.9	158.78	0.9682	157.21	0.9643	184.43	0.9969	183.13	0.9966	244.09	0.9991	244.10	0.9990
Average	161.81		161.18		193.19		192.93		224.99		224.59	

and $G(\alpha)/G(0.5)$ were compared for each sub-stage at 10 °C/min (Fig. 4d–f). The $P(u)/P(u_{0.5})$ plots of the sub-stages 1 and 2 were close to D3 and F2 of the theoretical master-plots, respectively. The values of E_a and R^2 obtained by the different pyrolysis mechanisms are provided in Table 4. E_a values of D3 (159.94 kJ/mol) and F2 (192.35 kJ/mol) were also consistent with the model-free methods. Therefore, the combination of the close $P(u)/P(u_{0.5})$ plots and the E_a values pointed to D3 and F2 as the best-fit mechanisms to describe the kinetics of sub-stages 1 and 2. However, the final sub-stage was located in between the theoretical master-plots F2 and F3, thus indicating that the Fn model $f(\alpha) = (1-\alpha)^n$ best described the kinetic process of this sub-stage.

3.2.3. Reaction order and pre-exponential factor

The last section showed that the first and two sub-stages had a determinate mechanism. To determine the reaction mechanism of the last sub-stage, the expression $f(\alpha) = (1-\alpha)^n$ when introduced into Eq. (8) became thus:

$$G(\alpha) = \frac{AE}{\beta R}P(u) = \frac{(1-\alpha)^{1-n}-1}{n-1} \tag{12}$$

To further test its optimal value, n was increased from 2.0 to 3.0 with an increment of 0.1 and a plot of $[(1-\alpha)^{1-n}-1]/(n-1)$ versus $EP(u)/\beta R$ was fitted a least-square regression line. The most potential n value for the three sub-stages were estimated with the closest zero intercept (Fig. 5a–c). The kinetic triplets of E_a, A, and $f(\alpha)$ for the three sub-stages of the main WT pyrolysis at 5, 10, 20 and 40 °C/min are shown in Table 5. The corresponding model functions were $f(\alpha) = (3/2)(1-\alpha)^{2/3}[1-(1-\alpha)^{1/3}]^{-1}$; $f(\alpha) = (1-\alpha)^2$; and $f(\alpha) = (1-\alpha)^{2.5}$ for the sub-stages, respectively.

For the validation of kinetic results, Fig. 5d–f showed the comparison of calculated versus experimental conversion curves for the three sub-stages. The good fit between the calculated and experimental data indicated the accuracy of the kinetic analysis results to be used to design a pyrolysis-processing system for WT as the feedstock in the bioenergy sector.

3.3. TG-FTIR analyses

The online gas-phase characteristics as a function of the pyrolysis temperature were detected using the FTIR spectra [50]. The macromolecules of (hemi-)cellulose, and lignin are subjected to the reactions of cross-link polymerization and dehydrogenation oxidation during the pyrolysis process and are in turn accompanied by the production of small molecule gases [14,51]. Fig. 6a shows the 3-D FTIR diagram of the WT pyrolysis at 10 °C/min. The evolved gases at a peak value of 345.3 °C were identified using their characteristic absorbance (Fig. 6b). The gas products, and their functional groups are presented in Table 6.

The change in the absorbance intensity of the volatile components with the temperature rise is presented in Fig. 6c. The gas products of the WT pyrolysis were generated mainly in the devolatilization stage corresponding to the range of 180 to 530 °C. At a lower temperature, all volatiles components appeared to originate mainly from hemi-cellulose. The concentrations of the gaseous products increased remarkably with the increased temperature. This was because cellulose, and partially,

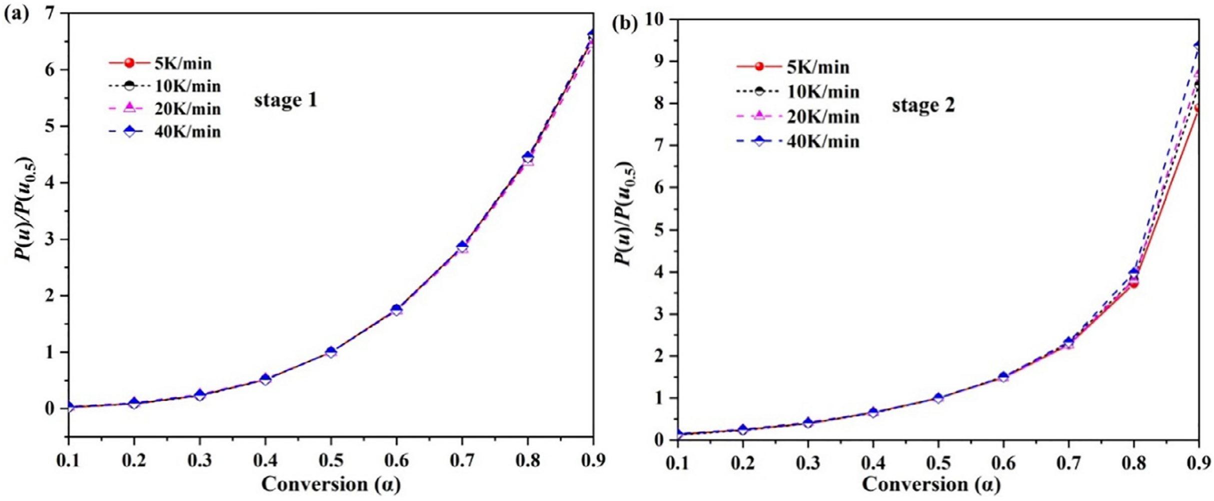

Fig. 4. $P(u)/P(u_{0.5})$ versus conversion degree for the four heating rates and the sub-stages of the WT pyrolysis (a) 1, (b) 2 and (c) 3; and $G(\alpha)/G(0.5)$ versus conversion degree for the 15 reaction models and the sub-stages of the WT pyrolysis (d) 1, (e) 2 and (f) 3 at 10 °C/min.

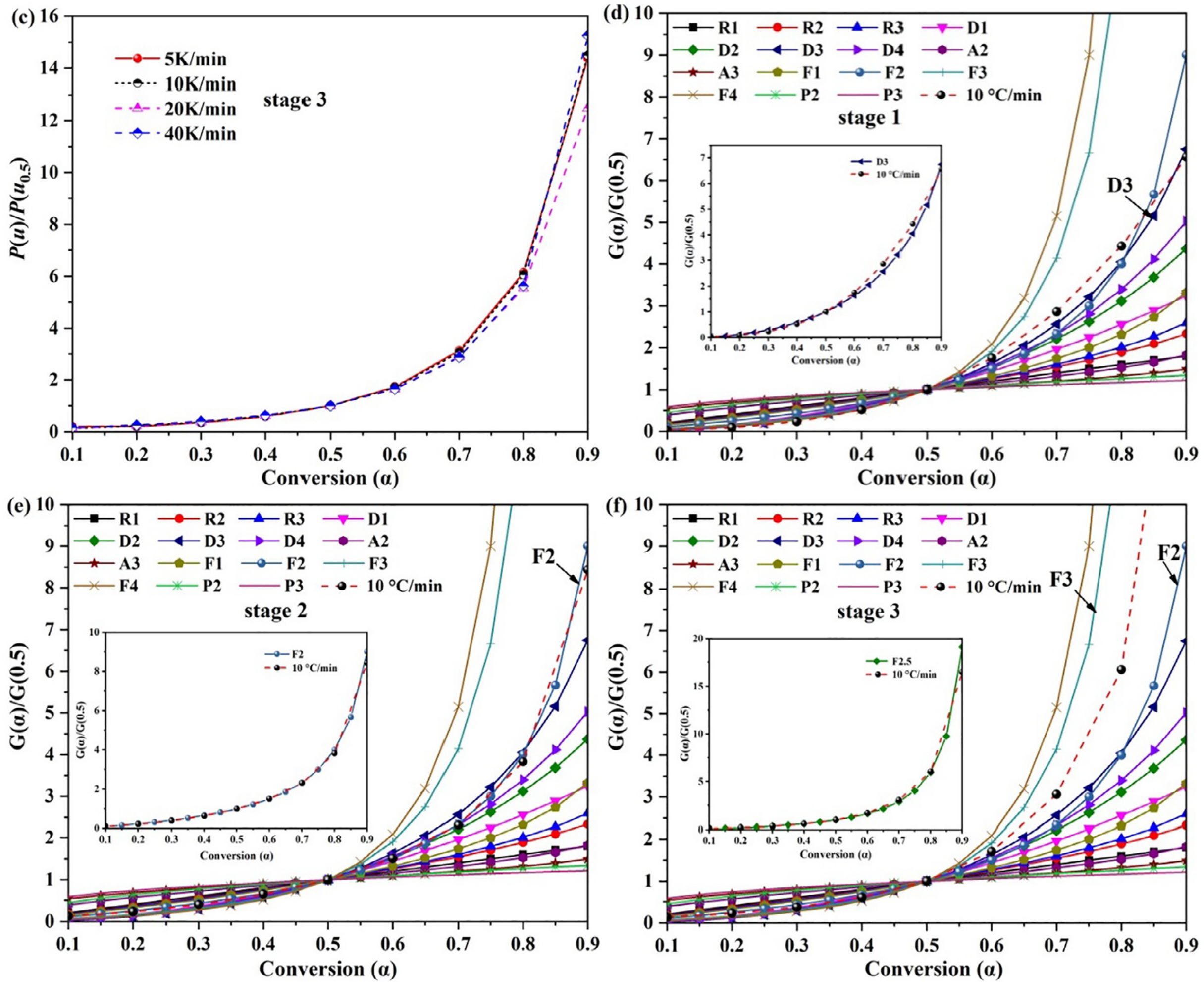

Fig. 4. (*continued*)

Table 4

E_a values (kJ/mol) of various pyrolysis mechanisms estimated by master-plots for the three sub-stages at 10 °C/min.

Mechanism	Stage 1		Stage 2		Stage 3	
	E_a	R^2	E_a	R^2	E_a	R^2
D1	125.97	0.9831	184.00	0.9336	157.97	0.8848
D2	138.94	0.9910	207.87	0.9536	180.19	0.9132
D3	159.94	0.9958	238.50	0.9730	208.86	0.9419
D4	144.88	0.9932	217.94	0.9610	189.62	0.9240
F1	82.22	0.9958	130.70	0.9847	114.07	0.9585
F2	113.82	0.9763	192.35	0.9989	172.12	0.9931
F3	97.06	0.9892	269.20	0.9897	244.72	0.9955
A2	36.57	0.9947	60.23	0.9818	51.13	0.9481
A3	21.36	9.9931	36.75	0.9779	30.15	0.9338
P2	24.68	0.9696	38.33	0.9056	30.65	0.8194
P3	13.44	0.9560	22.15	0.8770	16.49	0.7450
P4	7.81	0.9265	14.05	0.8346	9.42	0.6261
R1	58.45	0.9801	86.89	0.9257	73.08	0.9673
R2	69.37	0.9932	106.61	0.9612	91.49	0.9203
R3	73.43	0.9952	114.14	0.9704	98.54	0.9348

lignin began to disintegrate. In the higher temperature, the relative concentrations of volatiles components decreased gradually due to the degradation of lignin and cokes with low reaction activity. This was in line with the fact that the reactions occur at the higher temperatures with higher apparent activation energy when the recalcitrant materials are involved [42].

The peaks with the bands of 4000 to 3500 cm^{-1} indicated the releases of H_2O from the pyrolysis process [32]. The main release temperature of H_2O was in the range of 180 to 530 °C. H_2O was released mainly from the evolution of bulk water, bound water, and crystallization water in the mineral substance of the samples as well as from the cracking or reaction of oxygen functional groups in the pyrolysis process with the temperature rise [14,30].The absorbance peak in the range of 3115–2675 cm^{-1} was related to the release of CH_4, with 2359 cm^{-1} to the release of CO_2. The release of CH_4 can be attributed to the cracking of methoxyl–O–CH_3, which consists of hemi-cellulose, cellulose, and lignin. The yield of CH_4 rose greatly with the elevated pyrolysis temperature. The presence of a more obvious peak at 436 °C corresponding to the lignin pyrolysis may be caused by the abundant O—CH_3 content of lignin. CH_4 was reported to be generated as a result of several reactions during the pyrolysis thus: the free radical reaction ($CH_2/CH_3 + H \rightarrow CH_4$) at the low temperatures; and the thermal degradations of methoxyl–O–CH_3 [52] and benzyl groups at the higher temperatures [42]. The CO_2 release occurred due to the cracking and reforming of functional groups of carboxyl (C═O) and COOH, the cracking and abscission of C—C and C—O bonds connected with the main branch of hemi-cellulose, the cracking of C═O groups in cellulose, and the breaking of lateral C—C bonds [52]. A weak peak of CO_2 between 600 and 800 °C was attributed to the secondary degradation of C═O and C—O compounds, thus leading to the breaking chains and the reforming reactions. The absorbance waves between 2240 and 2060 cm^{-1} were related to the release of CO. The CO was detected although its concentration was not obvious. It was produced mainly by the degradation of carbonyl (C—O—C) and carboxyl (C═O) with poor

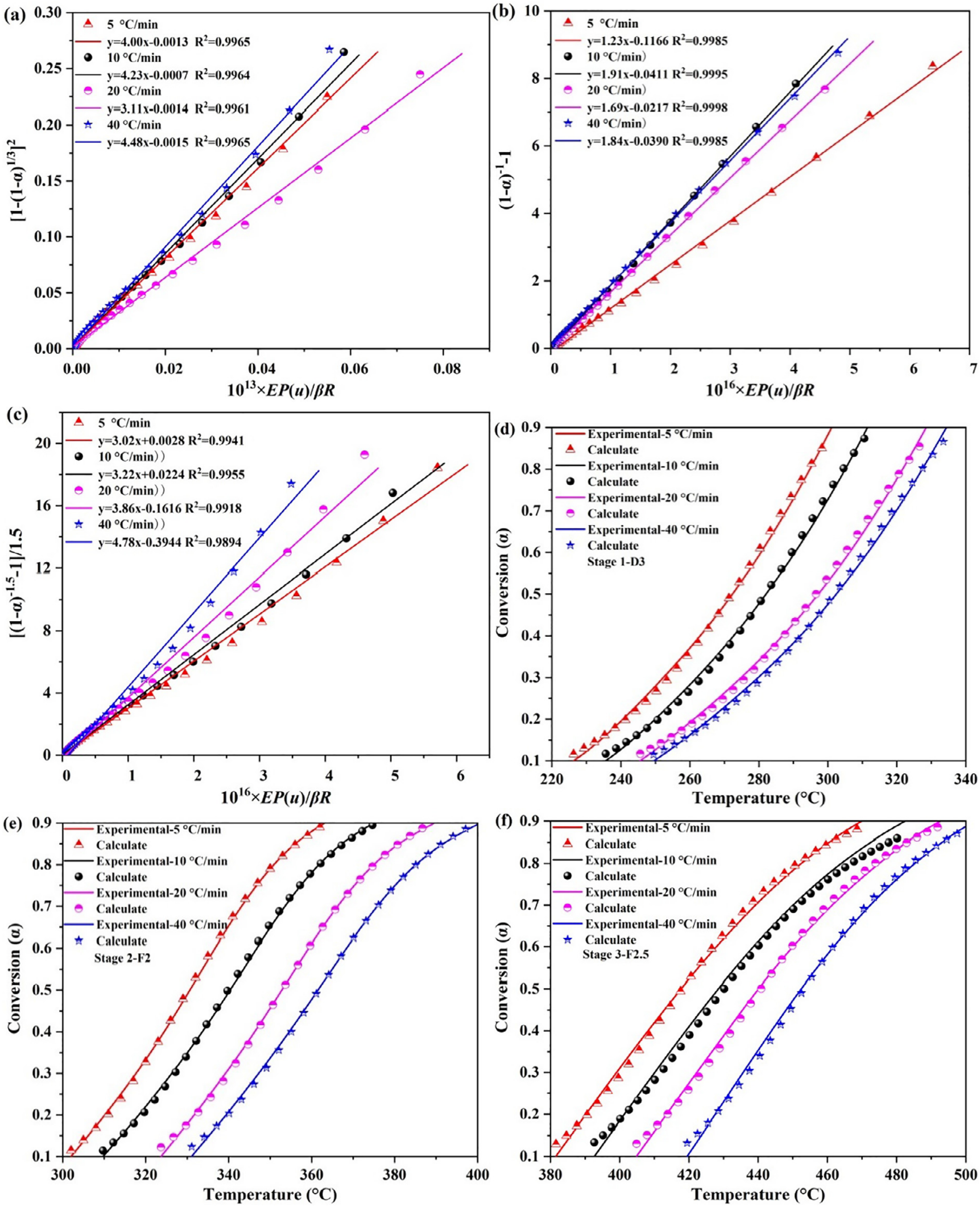

Fig. 5. (a-c) plotting $G(\alpha)$ versus $10^x \times EP(u)/\beta R$ for the three sub-stages of the WT pyrolysis; (d-f) calculated and experimental conversion data for the three sub-stages at the four heating rates.

thermal stability. The release of CO grew with the increased pyrolysis temperature. CO increased slowly again at above 730 °C due to the boudouard reaction of coke and CO_2 ($C + CO_2 \rightarrow 2CO$). The source of carbon oxide was shown to form from the ether bridges joining the lignin sub units at lower temperatures, and the dissociation of diaryl ether at higher temperatures [27].

The absorbance peak of C=O stretching in the region of 1900 to 1600 cm^{-1} corresponded to aldehyde, organic acid, and ketone produced by the splitting of epoxy group (−CH(O)CH−) [37]. Phenols with benzene ring group and hydroxyl group can be identified through the C−C skeleton vibration (1600–1450 cm^{-1}). The bending vibration at 1400–1300 cm^{-1} and the stretching vibration at 1200–1000 cm^{-1} were due to the hydroxyl group (C−O (H)) compounds. The releases of C=O, −OH, and C−O(H) such as carbonyls, acids, ether, phenol, and alcohol occurred mainly between 180 and 500 °C. The peak of absorbance at 966 cm^{-1} was due to the NH_3.

Table 5
Estimation of kinetic triplets of E_a, A, and $f(\alpha)$ for the three sub-stages of the main WT pyrolysis at four heating rates by master-plots.

Stage	β	E	A	$f(\alpha)$	R^2
	°C/min	kJ/mol	s^{-1}		
1	5	161.50	4.00×10^{13}	$(3/2)(1-\alpha)^{2/3}[1-(1-\alpha)^{1/3}]^{-1}$	0.9965
	10		4.23×10^{13}	$(3/2)(1-\alpha)^{2/3}[1-(1-\alpha)^{1/3}]^{-1}$	0.9964
	20		3.11×10^{13}	$(3/2)(1-\alpha)^{2/3}[1-(1-\alpha)^{1/3}]^{-1}$	0.9961
	40		4.49×10^{13}	$(3/2)(1-\alpha)^{2/3}[1-(1-\alpha)^{1/3}]^{-1}$	0.9965
2	5	193.11	1.30×10^{16}	$(1-\alpha)^2$	0.9985
	10		1.91×10^{16}	$(1-\alpha)^2$	0.9995
	20		1.69×10^{16}	$(1-\alpha)^2$	0.9998
	40		1.84×10^{16}	$(1-\alpha)^2$	0.9985
3	5	224.79	3.02×10^{16}	$(1-\alpha)^{2.5}$	0.9941
	10		3.22×10^{16}	$(1-\alpha)^{2.5}$	0.9955
	20		3.86×10^{16}	$(1-\alpha)^{2.5}$	0.9918
	40		4.78×10^{16}	$(1-\alpha)^{2.5}$	0.9894

In summary, the main gaseous products of the WT pyrolysis were identified as H_2O, CH_4, CO_2, C=O, phenol, C–O, and NH_3, and to a lesser extent CO. Overall, the release concentrations of the pyrolysis products were reported to be represented by the peak intensity of a specific wavenumber [53]. The summed integral values of emissions of the gas products are provided in Fig. 6d. The concentrations of these eight components were of the following order: CO_2 > C=O > phenol > CH_4 > C–O > NH_3 > H_2O > CO. Since the results of the TG-FTIR analyses needed to be confirmed, the Py-GC/MS analysis was provided for confirmation, and more detailed information about the products.

3.4. Py-GC-MS analysis

The total ion intensity of the gases evolved from the WT pyrolysis is presented using Py-GC/MS in Fig. 7. The products of the WT pyrolysis,

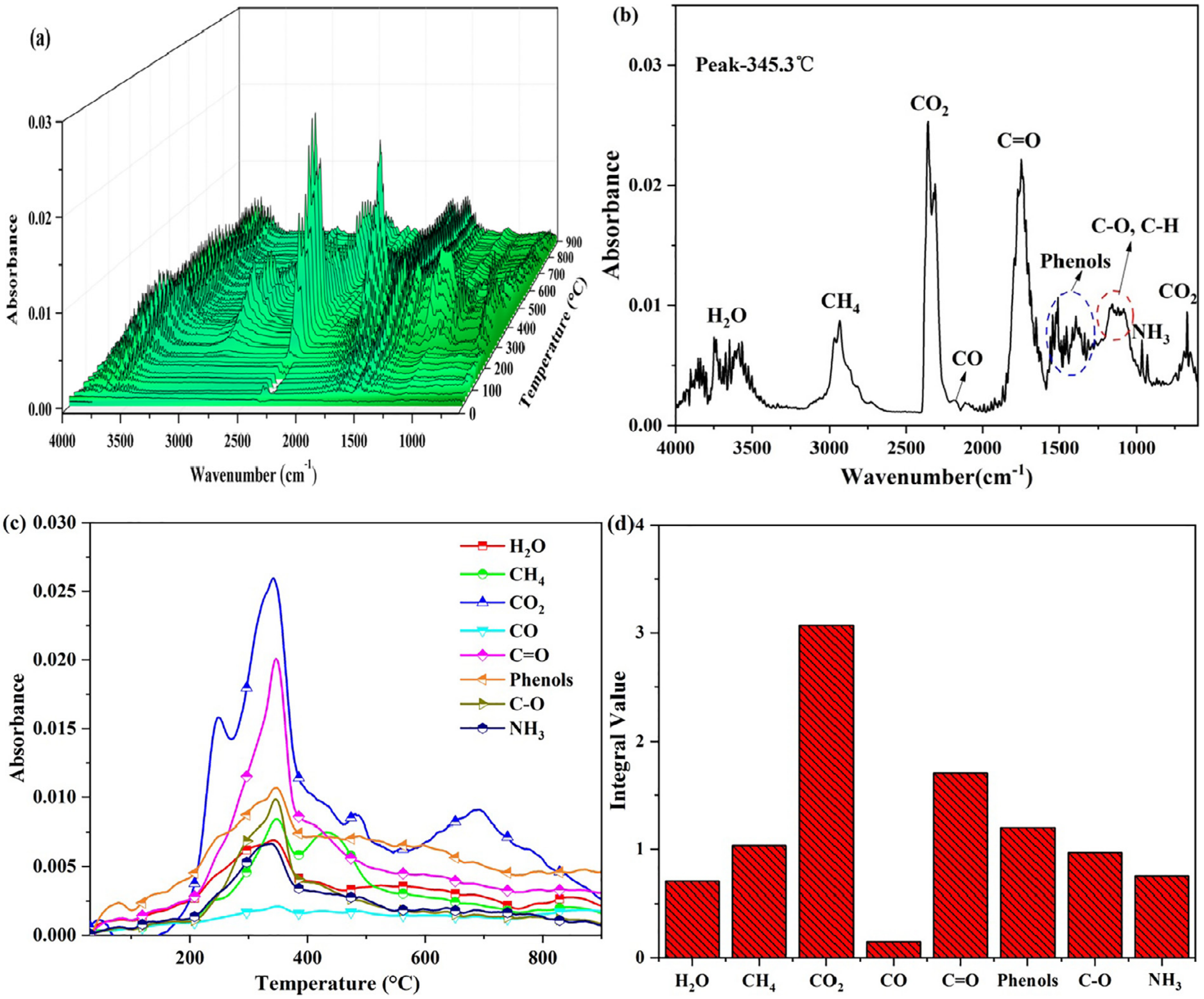

Fig. 6. (a) 3D infrared spectrum; (b) TG-FTIR spectrum for volatiles at a peak value of 345.3 °C; (c) absorbance of volatiles as a function of temperature; and (d) yield of emissions for WT pyrolysis.

Table 6
Main functional groups identified using TG-FTIR.

Wavenumber (cm^{-1})	Functional group	Vibration	Product
4000–3500, 1600–1300	O—H	Stretch, bending	H_2O
3115–2675	C—H	Stretch	CH_4
2400–2240, 680–660	C═O	Stretch, bending	CO_2
2240–2060	C—O	Stretch	CO
1900–1600	C═O	Stretch	Carbonyls, Acid
1600–1450, 1300–1200	C═C, O—H	Bending, stretch	Phenols
1400–1300, 1200–1000	C—O(H)	Stretch	Ether, Alcohol
966	N—H	Stretch	NH_3

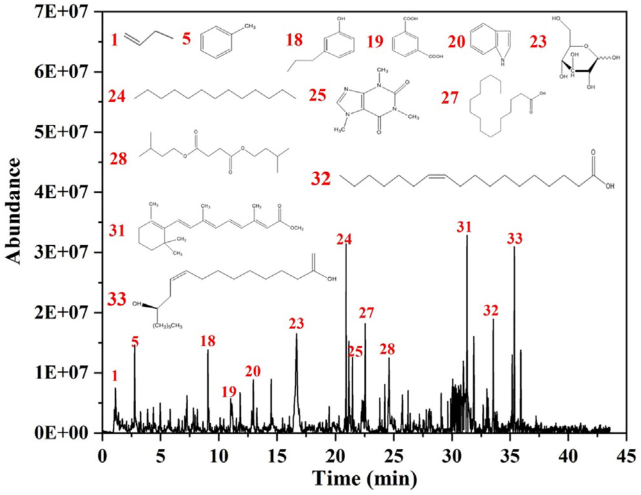

Fig. 7. Py-GC/MS detection of gas products evolved from the WT pyrolysis.

and their chemical compositions according to the NIST MS library are listed in Table 7. We mainly found the seven compound families of acid, benzene, furan, ketone, phenol, ester, and nitride. C═O (including acid, ester, ketone, and aldehyde) was the main product, as with the TG-FTIR result. The resultant products from the devolatilization of organic compounds can be either used to generate heat and electricity or transformed into chemicals via subsequent pathways [50].

The acids and ketones were previously demonstrated to result from the hemi-cellulose degradation, while phenols and aldehydes were due to the lignin degradation [13]. There existed a total of 33 organic compounds based on Py-GC/MS, including alkene, acid, benzene, furan, ketone, phenol, nitride, alcohol, aldehyde, alkyl, and ester. The precipitated species mainly included D-glucopyranoside-D-glucopyranosyl (peak 23), tridecylene (peak 24), caffeine (peak 25), hexadecanoic acid (peak 27), and ricinoleic acid (peak 33). Caffeine was detected as the pyrolysis product since the tea products contained a certain amount of caffeine [54]. Toluene, phenol, 4-propyl-, hexancdioic acid, bis(2-methylpropyl) ester, retinoic acid, methyl ester, and octadecenoic acid were some of the other compounds found in smaller amounts in the pyrolysis process. Yang et al. [55] found some similar compounds such as P-xylene, indole, toluene, and hexadecanoic acid from the pyrolysis of hazardous biological waste. The pyrolysis products of bagasse were found to include ketones, carboxylic acid, aldehydes, esters, alcohols, and benzene due to crackings, lignin polymerizations, and cellulose condensations [47]. Methylindole, careen, and benzenediol were also detected with the products since they were often added to tea as spices [56].

Overall, hemi-cellulose was shown to exhibit the following pyrolysis pathways: depolymerization, dehydration to furan and pyran ring derivatives, and furanose and pyranose ring-breakage to light oxygenated species. The primary pyrolysis of cellulose consisted of the following two similar stages: depolymerize to form anhydrosugars, and pyranose ring- breakage to light oxygenated species [27]. Lignin, made of the

Table 7
The classification and peak-area percentage of WT pyrolytic products based on Py-GC/MS.

Label	m/z	Molecular formula	Family	Compound	*t* (min)	Area (%)
1	56	C_4H_8	Alkene	Butene	1.12	2.09
2	60	$C_2H_4O_2$	Acid	Acetic acid	1.52	0.44
3	78	C_6H_6	Benzene	Benzene	1.71	0.49
4	96	C_6H_8O	Furan	2, 5-Dimethyl-furan	2.08	0.44
5	92	C_7H_8	Benzene	Toluene	2.77	4.19
6	112	C_8H_{16}	Alkene	Octene	3.14	0.69
7	113	$C_7H_{15}N$	Nitride	Ethyl-piperidine	3.27	1.18
8	93	C_6H_7N	Kctone	Methyl-pyridone	3.53	0.37
9	82	C_5H_6O	Furan	2-Methyl- Furan	3.88	1.17
10	106	C_8H_{10}	Benzene	1,3-Dimethyl-benzene	4.38	1.18
11	106	C_8H_{10}	Benzene	P-Xylene	4.96	1.75
12	112	$C_7H_{12}O$	Kctone	Methyl-cyclohexanone	5.82	0.87
13	110	$C_6H_6O_2$	Phenol	Benzenediol	6.87	0.40
14	140	$C_{10}H_{20}$	Alkene	Decene	7.07	0.70
15	108	C_7H_8O	Phenol	4-methyl-phenol	7.21	0.66
16	112	$C_6H_8O_2$	Kctone	2-Hydroxy-3-methyl-cylopent-2-enone	7.97	0.66
17	116	C_9H_8	Benzene	Indene	8.15	1.01
18	136	$C_9H_{12}O$	Phenol	Phenol, 4-propyl-	9.07	3.79
19	166	$C_8H_6O_4$	Acid	Benzene-1,3-dicarboxylic acid	11.83	2.56
20	117	C_7H_8N	Nitride	Indole	12.97	2.49
21	136	$C_9H_{12}O$	Phenol	Mehly-methylethy-phenol	13.28	1.23
22	131	C_9H_9N	Nitride	Methyl-indole	14.50	1.81
23	180	$C_6H_{12}O_6$	Aldehyde	D-Glucopyranoside,D-glucopyranosyl	16.69	21.62
24	184	$C_{13}H_{28}$	Alkyl	Tridecylene	20.89	6.89
25	194	$C_8H_{10}N_4O_2$	Nitride	Caffeine	21.13	5.43
26	240	$C_{16}H_{32}O$	Alcohol	9-Hexadecen-1-ol,(Z)-	21.44	3.23
27	256	$C_{16}H_{32}O_2$	Acid	Hexadecanoic acid	22.54	5.15
28	258	$C_{14}H_{26}O_4$	Ester	Hexancdioic acid, bis(2-methylpropyl) ester	24.59	4.37
29	296	$C_{19}H_{36}O_2$	Aldehyde	9-Octadecenoic acid (Z)-	25.74	1.99
30	258	$C_{14}H_{26}O_4$	Ester	Dodecanedioic acid, dimethyl ester	29.07	0.97
31	314	$C_{21}H_{30}O_2$	Ester	Retinoic acid, methyl ester	31.30	5.03
32	284	$C_{18}H_{36}O_2$	Acid	Octadecenoic acid	33.55	5.05
33	298	$C_{18}H_{34}O_3$	Acid	Ricinoleic acid	35.37	9.62

irregular array of differently bonded hydroxyl- and methoxy-substituted phenyl-propane units, is a complex, heterogeneous, three-dimensional polymer. Lignin structure showed intense structural transformations with the following degradation reactions: (1) the lignin β-O-4 bonds cleaving, (2) severe re-condensation reactions, (3) vinyl ether structures forming by the loss of the terminal hydroxymethyl groups from lignin side chains, and (4) the oxidative cleavage of the Cα-Cβ benzylic bonds with the formation of benzoic acid and benzoic aldehyde end groups [13]. Since benzene rings are not easy to break during the pyrolysis, the organic matter mainly comes from pyran rings of glucopyranose monomer and breaking of C—C bond on the rings [14]. The resultant pyrolysis products can be used as the main bioenergy intermediates and chemical substances.

4. Conclusion

In this study, the behaviors, kinetics, and products of the pyrolysis of waste tea were quantified. Out of the three stages of the thermal degradation, the main stage belonged to devolatilization between 187.0 and 536.5 °C. Our kinetic analysis indicated that the best-fit models were $f(\alpha) = (3/2)(1-\alpha)^{2/3}[1-(1-\alpha)^{1/3}]^{-1}$, $f(\alpha) = (1-\alpha)^2$ and $f(\alpha) = (1-\alpha)^{2.5}$ for the sub-stages of devolatilization, respectively. The main gaseous products of the WT pyrolysis based on TG-FTIR were identified as H_2O, CH_4, CO_2, C═O (acid anhydride, ketone or aldehyde), phenol, C—O, NH_3, and CO. The pyrolytic volatile products based on Py-GC/MS during the fast thermal cracking consisted of the seven compound families of acid, benzene, furan, ketone, phenol, ester, and nitride. The product species mainly included D-glucopyranoside-D-glucopyranosyl, tridecylene, caffeine, hexadecanoic acid, and ricinoleic acid. Overall, all the quantifications in this study are important to meeting the optimization and upscaling challenges of sustainable bioenergy production via the pyrolysis of waste tea in the power and industrial sectors integrated with carbon capture and storage technologies. The reaction models, and the pyrolysis products can provide some baselines and insights in order for the pyrolysis technologies in the industries to utilize waste tea as an alternative solid fuel. This low-cost and abundant biomass may be used to generate bioenergy and chemicals in a cost-efficient and ecofriendly way.

Declaration of interest

None.

Acknowledgments

This research was financially supported by National Natural Science Foundation of China (No. 51608129) and the Science and Technology Planning Project of Guangdong Province, China (Nos. 2016A050502059, 2019B020208017 & 2018A050506046). We would like to thank the teacher Yu from School of Light Industry and Chemical Engineering for providing TG guidance.

References

[1] Biswas B, Pandey N, Bisht Y, Singh R, Kumar J, Bhaskar T. Pyrolysis of agricultural biomass residues: comparative study of corn cob, wheat straw, rice straw and rice husk. Bioresour Technol 2017;237:57–63. https://doi.org/10.1016/j.biortech.2017.02.046.

[2] Li L, Wang G, Wang S, Qin S. Thermogravimetric and kinetic analysis of energy crop Jerusalem artichoke using the distributed activation energy model. J Therm Anal Calorim 2013;114(3):1183–9. https://doi.org/10.1007/s10973-013-3115-2.

[3] Xu C, Hu S, Xiang J, Zhang L, Sun L, Shuai C, et al. Interaction and kinetic analysis for coal and biomass co-gasification by TG-FTIR. Bioresour Technol 2014;154:313–21. https://doi.org/10.1016/j.biortech.2013.11.101.

[4] Hu M, Wang X, Chen J, Yang P, Liu C, Xiao B, et al. Kinetic study and syngas production from pyrolysis of forestry waste. Energy Convers Manage 2017;135:453–62. https://doi.org/10.1016/j.enconman.2016.12.086.

[5] Daioglou V, Stehfest E, Wicke B, Faaij A, van Vuuren DP. Projections of the availability and cost of residues from agriculture and forestry. GCB Bioenergy 2016;8(2):456–70. https://doi.org/10.1111/gcbb.12285.

[6] Welfle A, Gilbert P, Thornley P. Securing a bioenergy future without imports. Energy Policy 2014;68:1–14. https://doi.org/10.1016/j.enpol.2013.11.079.

[7] Fan S, Tang J, Wang Y, Li H, Zhang H, Tang J, et al. Biochar prepared from co-pyrolysis of municipal sewage sludge and tea waste for the adsorption of methylene blue from aqueous solutions: kinetics, isotherm, thermodynamic and mechanism. J Mol Liq 2016;220:432–41. https://doi.org/10.1016/j.molliq.2016.04.107.

[8] Zhao T, Chen Z, Lin X, Ren Z, Li B, Zhang Y. Preparation and characterization of microcrystalline cellulose (MCC) from tea waste. Carbohyd Polym 2018;184:164–70. https://doi.org/10.1016/j.carbpol.2017.12.024.

[9] Ahmed ST, Lee JW, Mun HS, Yang CJ. Effects of supplementation with green tea by-products on growth performance, meat quality, blood metabolites and immune cell proliferation in goats. J Anim Physiol An N 2015;99(6):1127–37. https://doi.org/10.1111/jpn.12279.

[10] Qing W, Chen K, Wang Y, Liu X, Lu M. Green synthesis of silver nanoparticles by waste tea extract and degradation of organic dye in the absence and presence of H_2O_2. Appl Surf Sci 2017;423:1019–24. https://doi.org/10.1016/j.apsusc.2017.07.007.

[11] Shen B, Tian L, Li F, Zhang X, Xu H, Singh S. Elemental mercury removal by the modified bio-char from waste tea. Fuel 2017;187:189–96. https://doi.org/10.1016/j.fuel.2016.09.059.

[12] Ahmad MS, Mehmood MA, Al Ayed OS, Ye G, Luo H, Ibrahim M, et al. Kinetic analyses and pyrolytic behavior of Para grass (Urochloa mutica) for its bioenergy potential. Bioresour Technol 2017;224:708–13. https://doi.org/10.1016/j.biortech.2016.10.090.

[13] Chen W-H, Wang C-W, Kumar G, Rousset P, Hsieh T-H. Effect of torrefaction pretreatment on the pyrolysis of rubber wood sawdust analyzed by Py-GC/MS. Bioresour Technol 2018;259:469–73. https://doi.org/10.1016/j.biortech.2018.03.033.

[14] Liang F, Wang R, Hongzhong X, Yang X, Zhang T, Hu W, et al. Investigating pyrolysis characteristics of moso bamboo through TG-FTIR and Py-GC/MS. Bioresour Technol 2018;256:53–60. https://doi.org/10.1016/j.biortech.2018.01.140.

[15] Ma Z, Chen D, Gu J, Bao B, Zhang Q. Determination of pyrolysis characteristics and kinetics of palm kernel shell using TGA–FTIR and model-free integral methods. Energy Convers Manage 2015;89:251–9. https://doi.org/10.1016/j.enconman.2014.09.074.

[16] Zou S, Wu Y, Yang M, Li C, Tong J. Pyrolysis characteristics and kinetics of the marine microalgae Dunaliella tertiolecta using thermogravimetric analyzer. Bioresour Technol 2010;101(1):359–65. https://doi.org/10.1016/j.biortech.2009.08.020.

[17] Yahya NY, Ngadi N, Wong S, Hassan O. Transesterification of used cooking oil (UCO) catalyzed by mesoporous calcium titanate: kinetic and thermodynamic studies. Energy Convers Manage 2018;164:210–8. https://doi.org/10.1016/j.enconman.2018.03.011.

[18] Tang Y, Ma X, Wang Z, Wu Z, Yu Q. A study of the thermal degradation of six typical municipal waste components in CO_2 and N_2 atmospheres using TGA-FTIR. Thermochim Acta 2017;657:12–9. https://doi.org/10.1016/j.tca.2017.09.009.

[19] Ghadikolaei SS, Omrani A, Ehsani M. Non-isothermal degradation kinetics of Ethylene-Vinyl Acetate Copolymer nanocomposite reinforced with modified Bacterial Cellulose Nanofibers using advanced isoconversional and master plot analyses. Thermochim Acta 2017;655:87–93. https://doi.org/10.1016/j.tca.2017.06.014.

[20] Mishra RK, Mohanty K. Pyrolysis kinetics and thermal behavior of waste sawdust biomass using thermogravimetric analysis. Bioresour Technol 2018;251:63–74. https://doi.org/10.1016/j.biortech.2017.12.029.

[21] Xu F, Wang B, Yang D, Hao J, Qiao Y, Tian Y. Thermal degradation of typical plastics under high heating rate conditions by TG-FTIR: pyrolysis behaviors and kinetic analysis. Energy Convers Manage 2018;171:1106–15. https://doi.org/10.1016/j.enconman.2018.06.047.

[22] Yahyaoui R, Jimenez PES, Maqueda LAP, Nahdi K, Luque JMC. Synthesis, characterization and combined kinetic analysis of thermal decomposition of hydrotalcite ($Mg_6Al_2(OH)_{16}CO_3{\cdot}4H_2O$). Thermochim Acta 2018;667:177–84. https://doi.org/10.1016/j.tca.2018.07.025.

[23] Chen J, Song X, Mu L, Li A, Yin H. Thermogravimetric analysis and kinetics of the combustionof refining and chemicals wastewater in different oxygenconcentrations. J Therm Anal Calorim 2015;119:2205–19. https://doi.org/10.1007/s10973-014-4373-3.

[24] Xie C, Liu J, Xie W, Kuo J, Lu X, Zhang X, et al. Quantifying thermal decomposition regimes of textile dyeing sludge, pomelo peel, and their blends. Renew Energy 2018;122:55–64. https://doi.org/10.1016/j.renene.2018.01.093.

[25] Lin Y, Liao Y, Yu Z, Fang S, Lin Y, Fan Y, et al. Co-pyrolysis kinetics of sewage sludge and oil shale thermal decomposition using TGA–FTIR analysis. Energy Convers Manage 2016;118:345–52. https://doi.org/10.1016/j.enconman.2016.04.004.

[26] Zhao J, Xiuwen W, Hu J, Liu Q, Shen D, Xiao R. Thermal degradation of softwood lignin and hardwood lignin by TG-FTIR and Py-GC/MS. Polym Degrad Stabil 2014;108:133–8. https://doi.org/10.1016/j.polymdegradstab.2014.06.006.

[27] Gu X, Ma X, Li L, Liu C, Cheng K, Li Z. Pyrolysis of poplar wood sawdust by TG-FTIR and Py–GC/MS. J Anal Appl Pyrol 2013;102:16–23. https://doi.org/10.1016/j.jaap.2013.04.009.

[28] Chen J, Lang X, Wang Y, Li G, Yang Z, Fan S. Comparative evaluation of different non-condensable gases on thermal behaviors, kinetics, high pressure properties, and product characteristics of heavy oil. Energy Convers Manage 2018;162:13–25. https://doi.org/10.1016/j.enconman.2018.02.029.

[29] Soysa R, Choi YS, Kim SJ, Choi SK. Fast pyrolysis characteristics and kinetic study of Ceylon tea waste. Int J Hydrogen Energy 2016;41(37):16436–43. https://doi.org/

10.1016/j.ijhydene.2016.04.066.

[30] Tian L, Shen B, Xu H, Li F, Wang Y, Singh S. Thermal behavior of waste tea pyrolysis by TG-FTIR analysis. Energy 2016;103:533–42. https://doi.org/10.1016/j.energy.2016.03.022.

[31] Peng C, Liu J, Liu H, Zhou H, Gong J. Influence of different fermentation raw materials on pyrolyzates of Pu-erh tea theabrownin by Curie-point pyrolysis-gas chromatography-mass spectroscopy. Int J Biol Macromol 2013;54:197–203. https://doi.org/10.1016/j.ijbiomac.2012.12.021.

[32] Chen L, Yu Z, Liang J, Liao Y, Ma X. Co-pyrolysis of chlorella vulgaris and kitchen waste with different additives using TG-FTIR and Py-GC/MS. Energy Convers Manage 2018;177:582–91. https://doi.org/10.1016/j.enconman.2018.10.010.

[33] Hao J, Feng W, Qiao Y, Tian Y, Zhang J, Che Y. Thermal cracking behaviors and products distribution of oil sand bitumen by TG-FTIR and Py-GC/TOF-MS. Energy Convers Manage 2017;151:227–39. https://doi.org/10.1016/j.enconman.2017.08.083.

[34] Cai H, Zou H, Liu J, Xie W, Kuo J, Buyukada M, et al. Thermal degradations and processes of waste tea and tea leaves via TG-FTIR: combustion performances, kinetics, thermodynamics, products and optimization. Bioresour Technol 2018;268:715–25. https://doi.org/10.1016/j.biortech.2018.08.068.

[35] Xie C, Liu J, Zhang X, Xie W, Sun J, Chang K, et al. Co-combustion thermal conversion characteristics of textile dyeing sludge and pomelo peel using TGA and artificial neural networks. Appl Energy 2018;212:786–95. https://doi.org/10.1016/j.apenergy.2017.12.084.

[36] Jiang L, Zhang D, Li M, He J-J, Gao Z-H, Zhou Y, et al. Pyrolytic behavior of waste extruded polystyrene and rigid polyurethane by multi kinetics methods and Py-GC/MS. Fuel 2018;222:11–20. https://doi.org/10.1016/j.fuel.2018.02.143.

[37] Zhang Z, Wang C, Huang G, Liu H, Yang S, Zhang A. Thermal degradation behaviors and reaction mechanism of carbon fibre-epoxy composite from hydrogen tank by TG-FTIR. J Hazard Mater 2018;357:73–80. https://doi.org/10.1016/j.jhazmat.2018.05.057.

[38] Huang J, Liu J, Chen J, Xie W, Kuo J, Lu X, et al. Combustion behaviors of spent mushroom substrate using TG-MS and TG-FTIR: thermal conversion, kinetic, thermodynamic and emission analyses. Bioresour Technol 2018;266:389–97. https://doi.org/10.1016/j.biortech.2018.06.106.

[39] Chen J, Xie C, Liu J, He Y, Xie W, Zhang X, et al. Co-combustion of sewage sludge and coffee grounds under increased O_2/CO_2 atmospheres: thermodynamic characteristics, kinetics and artificial neural network modeling. Bioresour Technol 2018;250:230–8. https://doi.org/10.1016/j.biortech.2015.05.031.

[40] Chen R, Lu S, Zhang Y, Lo S. Pyrolysis study of waste cable hose with thermogravimetry/Fourier transform infrared/mass spectrometry analysis. Energy Convers Manage 2017;153:83–92. https://doi.org/10.1016/j.enconman.2017.09.071.

[41] Irmak Aslan D, Parthasarathy P, Goldfarb JL, Ceylan S. Pyrolysis reaction models of waste tires: application of Master-Plots method for energy conversion via devolatilization. Waste Manage 2017;68:405–11. https://doi.org/10.1016/j.wasman.2017.06.006.

[42] Chen J, Mu L, Jiang B, Yin H, Song X, Li A. TG/DSC-FTIR and Py-GC investigation on pyrolysis characteristics of petrochemical wastewater sludge. Bioresour Technol 2015;192:1–10. https://doi.org/10.1016/j.biortech.2015.05.031.

[43] Liu C, Liu J, Sun G, Xie W, Kuo J, Li S, et al. Thermogravimetric analysis of (co-) combustion of oily sludge and litchi peels: combustion characterization, interactions and kinetics. Thermochim Acta 2018;667:207–18. https://doi.org/10.1016/j.tca.2018.06.009.

[44] Selcuk N, Yuzbasi NS. Combustion behaviour of Turkish lignite in O_2/N_2 and O_2/CO_2 mixtures by using TGA–FTIR. J Anal Appl Pyrol 2011;90(2):133–9. https://doi.org/10.1016/j.jaap.2010.11.003.

[45] Uzun BB, Apaydin-Varol E, Ateş F, Özbay N, Pütün AE. Synthetic fuel production from tea waste: characterisation of bio-oil and bio-char. Fuel 2010;89(1):176–84. https://doi.org/10.1016/j.fuel.2009.08.040.

[46] Chen J, Wang Y, Lang X, Ren X, Fan S. Comparative evaluation of thermal oxidative decomposition for oil-plant residues via thermogravimetric analysis: thermal conversion characteristics, kinetics, and thermodynamics. Bioresour Technol 2017;243:37–46. https://doi.org/10.1016/j.biortech.2017.06.033.

[47] Lin Y, Liao Y, Yu Z, Fang S, Ma X. A study on co-pyrolysis of bagasse and sewage sludge using TG-FTIR and Py-GC/MS. Energy Convers Manage 2017;151:190–8. https://doi.org/10.1016/j.enconman.2017.08.062.

[48] Chandrasekaran A, Ramachandran S, Subbiah S. Determination of kinetic parameters in the pyrolysis operation and thermal behavior of Prosopis juliflora using thermogravimetric analysis. Bioresour Technol 2017;233:413–22. https://doi.org/10.1016/j.biortech.2017.02.119.

[49] Aslan DI, Ozogul B, Ceylan S, Geyikci F. Thermokinetic analysis and product characterization of Medium Density Fiberboard pyrolysis. Bioresour Technol 2018;258:105–10. https://doi.org/10.1016/j.biortech.2018.02.126.

[50] Fang S, Yu Z, Ma X, Lin Y, Chen L, Liao Y. Analysis of catalytic pyrolysis of municipal solid waste and paper sludge using TG-FTIR, Py-GC/MS and DAEM (distributed activation energy model). Energy 2018;143:517–32. https://doi.org/10.1016/j.energy.2017.11.038.

[51] Stefanidis SD, Kalogiannis KG, Iliopoulou EF, Michailof CM, Pilavachi PA, Lappas AA. A study of lignocellulosic biomass pyrolysis via the pyrolysis of cellulose, hemicellulose and lignin. J Anal Appl Pyrol 2014;105:143–50. https://doi.org/10.1016/j.jaap.2013.10.013.

[52] Ding Y, Ezekoye OA, Lu S, Wang C. Thermal degradation of beech wood with thermogravimetry/Fourier transform infrared analysis. Energy Convers Manage 2016;120:370–7. https://doi.org/10.1016/j.enconman.2016.05.007.

[53] Granada E, Eguía P, Vilan JA, Comesaña JA, Comesaña R. FTIR quantitative analysis technique for gases. Application in a biomass thermochemical process. Renew. Energy 2012;41:416–21. https://doi.org/10.1016/j.renene.2011.11.020.

[54] Sökmen Münevver, Demir Ezgi, Alomar SY. Optimization of sequential supercritical fluid extraction (SFE) of caffeine and catechins from green tea. J Supercrit Fluid 2018;133:171–6. https://doi.org/10.1016/j.supflu.2017.09.027.

[55] Yang S, Zhu X, Wang J, Jin X, Liu Y, Qian F, et al. Combustion of hazardous biological waste derived from the fermentation of antibiotics using TG-FTIR and Py-GC/MS techniques. Bioresour Technol 2015;193:156–63. https://doi.org/10.1016/j.biortech.2015.06.083.

[56] Zhu Y, Lv HP, Shao CY, Kang S, Zhang Y, Guo L, et al. Identification of key odorants responsible for chestnut-like aroma quality of green teas. Food Res Int 2018;108:74–82. https://doi.org/10.1016/j.foodres.2018.03.026.